Journal of Chromatography A, 1233 (2012) 100–108

Contents lists available at SciVerse ScienceDirect

Journal of Chromatography A

journal homepage: www.elsevier.com/locate/chroma

Operational-modes of field-flow fractionation in microfluidic channels

T.N. Shendruk*, G.W. Slater

University of Ottawa, Department of Physics, MacDonald Hall, 150 Louis-Pasteur, Ottawa, ON, K1N 6N5, Canada

ARTICLE INFO

Article history:
Received 12 October 2011
Received in revised form 21 January 2012
Accepted 23 January 2012
Available online 30 January 2012

Keywords:
Field-flow fractionation
Microfluidic separation
Faxén's law
Steric-mode FFF
Hydrodynamic chromatography

ABSTRACT

Through a careful consideration of the retention ratio for field-flow fractionation (FFF), we show that a single unified ideal retention theory can predict a wide range of separation behaviours including hydrodynamic chromatography, normal-mode FFF and steric-mode FFF by introducing the concept of a *device retention parameter*. We determine the critical device retention parameter above which normal-mode does not exist and there is no clear distinction between hydrodynamic chromatography and steric-mode FFF. Numerical analysis of the elution order as a function of particle size quantitatively predicts the transitions between these regimes. The resulting map of the operational-modes shows each of the regions and their connectivity, and so may guide future device design. By extending this analysis to account for the variation of stress over particle surfaces, a hitherto unreported regime called *Faxén-mode* FFF is predicted, which has the same elution order as normal-mode FFF. This mode arises when particle sizes approach the channel height, as can occur when microfluidic devices are utilized for FFF. The transition from steric-mode to Faxén-mode FFF is numerically mapped and approximations for each transition are presented.

1. Introduction

Field-flow fractionation (FFF) is an elegant separation technique based on a simple concept: separation of a mixture of different species can occur when solute particles, carried through a channel by a nonuniform, laminar flow profile, are acted on by an external field applied perpendicular to the flow. A schematic demonstrating the principles of FFF is given in Fig. 1 for the case of a symmetric parabolic flow profile. The perpendicular field pushes the ensemble of solutes against the accumulation wall but diffusion disperses the solute and resists the inhomogeneity. An exponential concentration distribution results in equilibrium. In particular, each species of solute has a different concentration profile. Since solute particles near the channel wall are subject to slower flowing solvent than particles near the centre, samples with a mean height close to the accumulation wall are carried along with a slower average velocity than samples with a larger mean height.

The simplicity of FFF disguises the flexibility of the technique. FFF has been used to separate particles as small as 1 nm [1–4] and as large as 100 μm [5,6]. It has been used to size separate everything from colloids [7–10] to macromolecules [11–15] to cells [16–19]. It can do this because of the wide variety of fields that can be used. Sedimentation, cross flows (both symmetrical and asymmetrical), and thermal fields are most commonly used. However, electrical, pressure, magnetic, dielectrophoretic, acoustic, photophoretic have all been demonstrated as acceptable physical fields [20,21]. The miniaturization of FFF techniques for wide-spread use in microfluidic devices appears tenable. Electrical- [22,23], dielectrophoretic- [24,25], and thermal- [26,27] FFF appear particularly amenable to micro- and nanofluidic devices [28,29]. However, miniaturization must be approached with caution. Effects due to miniaturization can be subtle and easily overlooked. The consequences of using microfluidic channels as FFF devices have been discussed in the literature [30–32]. Initial discussions centred on the role of channel dimensions in FFF [30]. In ideal situations, efficiency and speed are independent of channel height while selectivity is reduced with decreased channel height. At that time, there seemed to be a consensus that there was no immediate advantage to decreasing channel size.

More recently, it was pointed out that a subset of FFF techniques does in fact benefit from miniaturization. In particular, the resolution of electrical-FFF is increased as channel height is decreased, allowing for shorter analysis times in microchannels [31]. Improvements to both the resolution and the separation efficiency have been quantitatively demonstrated [32]. It is now recognized that in practice miniaturization entails both a decrease in channel height and also length which results in less peak spreading [32].

Experimentalists seeking to reap the benefits of using microfluidic channels in FFF apparatuses must recognize that, depending on sample and chosen channel height, the size of solute particles may vary from relatively small to large and confined. Although this does not necessarily preclude analytical interpretation of resulting chromatograms, it does require a unified retention theory that can

* Corresponding author. Tel.: +1 613 562 5800x6773; fax: +1 613 562 5190.
E-mail addresses: tshen098@uottawa.ca (T.N. Shendruk), gary.slater@uottawa.ca (G.W. Slater).

0021-9673/$ – see front matter.
doi:10.1016/j.chroma.2012.01.061

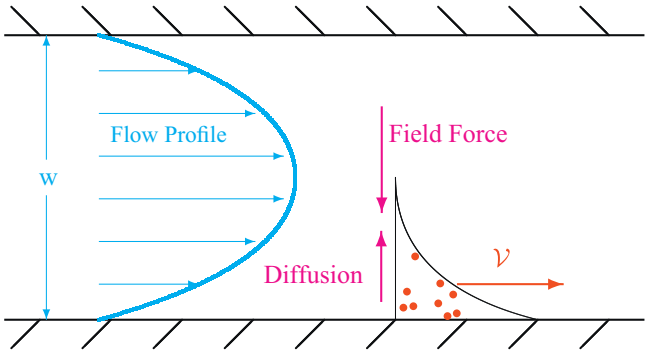

Fig. 1. Schematic of normal-mode FFF. An external force, perpendicular to the flow profile pushes the solute against the accumulation plate. The competition between the force and the diffusivity establishes a concentration gradient. The mean velocity of the solute $\langle \mathcal{V} \rangle$ is a function of the solute concentration $c(\tilde{y})$ and solvent velocity profiles $v(\tilde{y})$.

predict the fractionation for samples of everything from the tiniest tracer particles eluting in the hydrodynamic chromatograghy limit of FFF to the largest beads that fit snugly in the channel. In practice, a microscopic system size is needed for these two limits to be achieved in a single device.

In this paper, we take a simplistic view of the FFF process. We do not explicitly account for the fact that we are concerned with micro- and nanoscopic channel heights. Rather, we extend the traditional theory of Giddings [5,33,34] into operation regimes that at one time were quixotic but in today's age of microfluidics and nanotechnology are within reach. The theory is ideal in the sense that the flow field is assumed to be slow and unperturbed, and particles' interactions with the wall are assumed to be solely steric, without frictional or hydrodynamic interactions. Similarly, complicating effects such as particle slip, nonparabolic solvent flow and attraction to the accumulation wall are intently ignored [35].

2. Background

2.1. Normal-mode FFF

Consider a cross-sectional area with a solvent flow velocity field v parallel to the plates and solute concentration profile c. The cross-sectional average velocity of solute through a plane is

$$\langle \mathcal{V} \rangle = \frac{\langle cv \rangle}{\langle c \rangle} \tag{1}$$

where $\langle \cdot \rangle$ denotes cross-sectional average over the channel height. One should compare $\langle \mathcal{V} \rangle$ to the average velocity of the solute carrier fluid, $\langle v \rangle$. The retention ratio R is defined as the ratio of these two mean velocities. Since both elute through the same length of channel, the ratio of the time it takes the solute to elute (called the retention time) and the time it takes the solvent to elute (called the void time) is equivalent to the ratio of mean velocities as

$$R = \frac{t_0}{t_R} = \frac{\langle \mathcal{V} \rangle}{\langle v \rangle} = \frac{\langle cv \rangle}{\langle c \rangle \langle v \rangle}. \tag{2}$$

If no-slip at each wall is assumed and any distortion due to the perpendicular field is neglected, (*e.g.* thermal-FFF tends to skew the velocity profile [36,37,20]), the velocity of the fluid as a function of the distance from the accumulation wall normalized by the channel height $\tilde{y} = y/w$ (hereafter $\tilde{\cdot}$ denotes scaling by channel height, w) is given by the Poiseuille equation

$$v(\tilde{y}) = 6\langle v \rangle \left(\tilde{y} - \tilde{y}^2 \right). \tag{3}$$

Any perpendicular external force f can be used to create a nonuniform concentration distribution but we assume the concentration profile is independent of the mean flow velocity $\langle v \rangle$ [38].

Table 1
External forces f and corresponding scaling exponents α and device retention parameters Λ for examples of common FFF techniques. Variable names are the same as used by Cölfen and Antonietti in Table 1 of Ref. [20] with the notable exceptions that here the particle size is r, the centrifugal acceleration is G and the Stokes–Einstein equation $D = k_B T/6\pi\eta r$ has been used, where η is the solvent viscosity.

FFF-method	f	α	Λ
Sedimentation	$\frac{4\pi}{3} G \Delta\rho r^3$	3	$\frac{3}{4\pi} \frac{k_B T}{G\Delta\rho w^4}$
Flow	$6\pi\eta \frac{w\dot{V}_c}{V_0} r$	1	$\frac{k_B T}{6\pi\eta w^3} \frac{V_0}{\dot{V}_c}$
Thermal	$6\pi\eta \frac{D_T \Delta T}{w} r$	1	$\frac{k_B T}{6\pi w \eta D_T \Delta T}$
Magnetic	$\frac{4\pi}{3} \rho\chi_m H_m \Delta H_m r^3$	3	$\frac{3}{4\pi} \frac{k_B T}{w^4 \rho\chi_m H_m \Delta H_m}$
Electrical	$6\pi\eta\mu_e E r$	1	$\frac{k_B T}{6\pi\eta\mu_e E w}$

Point-particles in a solution with thermal energy of $k_B T$ have a concentration profile with the form

$$c(\tilde{y}) = c_0 \exp\left(-\frac{fy}{k_B T} \right) = c_0 \exp\left(-\frac{\tilde{y}}{\lambda} \right) \tag{4}$$

where c_0 is the concentration of solute at the accumulation wall, $\tilde{y} = 0$. The retention parameter λ is strictly defined as the ratio between the thermal and potential energy scales

$$\lambda \equiv \frac{k_B T}{fw}. \tag{5}$$

For point-particles, the mean concentration height thus has the form

$$\langle \tilde{y} \rangle = \frac{\langle \tilde{y} c \rangle}{\langle c \rangle} = \lambda + \frac{1}{1 - e^{1/\lambda}}. \tag{6a}$$

In the strong force limit, λ becomes small and

$$\langle \tilde{y} \rangle \simeq \lambda - e^{-1/\lambda} \simeq \lambda. \tag{6b}$$

In this limit, we can interpret λ as the dimensionless length scale of the concentration distribution. In the negligible force limit, λ is large and expanding the exponential in Eq. (6a) to third order leads to

$$\langle \tilde{y} \rangle \simeq \frac{1}{2} \left[1 - \frac{1}{6\lambda} + \frac{1}{360\lambda^3} + \cdots \right] \simeq \frac{1}{2} \tag{6c}$$

as we would expect for a uniform concentration.

In much the same way as was done for $\langle \tilde{y} \rangle$, an analytical expression for the retention ratio can be found by evaluating the averages in Eq. (2) for Eqs. (3) and (4). The resulting retention ratio is independent of flow rate:

$$R(\lambda) = 6\lambda \mathcal{L}\left(\frac{1}{2\lambda} \right) \tag{7}$$

where $\mathcal{L}(x) = \coth(x) - 1/x$ is the Langevin function. Eq. (7) has been shown to be very versatile for parameterizing retention [20,21] and characterizes what has been called *normal-mode* FFF.

Although the theory presented so far has treated the solute as an ensemble of point-particles, there is an implicit size dependence through λ. For instance, in sedimentation-FFF it is generally appropriate to assume a constant solute mass density such that the gravitational force f goes as the volume r^3 of the spherical particle or $\lambda \sim 1/f \sim r^{-3}$. To consider this in a general manner, let the force scale as the particle radius r to some power α such that the retention parameter can be rewritten

$$\lambda = \frac{k_B T}{\mu r^\alpha w} = \frac{k_B T}{\mu \tilde{r}^\alpha w^{1+\alpha}} = \Lambda \tilde{r}^{-\alpha}, \tag{8}$$

where we have extracted the normalized size dependence $\tilde{r}^\alpha$ from both the force ($f \equiv \mu r^\alpha$) and the retention parameter λ. The resulting dimensionless number, Λ, characterizes the FFF apparatus itself (for this reason it is called the *device retention parameter*) and is given for a few examples in Table 1.

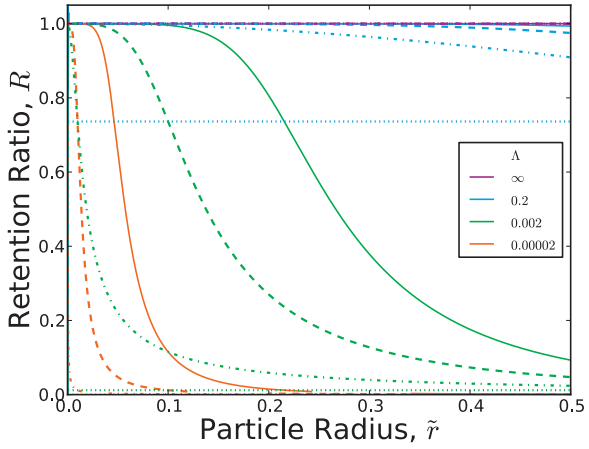

Fig. 2. Retention ratio $R(\tilde{r})$ as predicted by the standard point-particle theory for normal-mode FFF. The retention parameter λ is assumed to vary like $\lambda = \Lambda\tilde{r}^{-\alpha}$ but the particle size is otherwise not taken into account. Solid lines denote $\alpha = 3$, dashed $\alpha = 2$, dash-dot $\alpha = 1$ and dotted lines denote $\alpha = 0$ (all of which are horizontal). Small particles elute first except when $\alpha = 0$ where retention time is not a function of particle size.

Fig. 2 demonstrates that the point-particle theory of normal-mode FFF then predicts that small particles elute before large particles do. The monotonic decrease in elution time with particle size remains true for all device retention parameters Λ and all α-scaling. The magnitude of the slope increases as Λ is reduced, which is indicative of why the resolution increases with external force.

2.2. Steric-mode FFF

The steric interaction of finite-size solutes with the accumulation wall creates an excluded region as schematically shown in Fig. 3. To include the effects of steric repulsion from the wall, the integration limits on the profiles used to determine the retention ratio are altered. Steric effects are handled by stating that $c(\tilde{y})$ is the concentration profile of the centre of masses of the spherical particles of scaled radius $\tilde{r} = r/w$. The flow field is still assumed to be slow (low particle Reynolds number and insignificant inertial contributions) [39,40] and unperturbed by the presence of the solute (infinitely wide channels and dilute solutions) [41,42]. The variable c_0 is redefined as the concentration at the lowest point, *i.e.* a distance $\tilde{r}$ from the accumulation wall, so that the concentration profile becomes

$$c(\tilde{y}) = \begin{cases} c_0 e^{-(\tilde{y}-\tilde{r})/\lambda} & \text{for } \tilde{r} < \tilde{y} < 1-\tilde{r} \\ 0 & \text{otherwise} \end{cases} \tag{9}$$

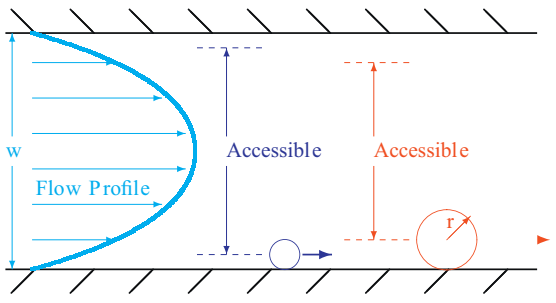

Fig. 3. Schematic representation of steric-mode FFF. When hard, finite-sized solutes undergo elution, they are excluded from a region near the wall where the fluid velocity is low. As a result, they tend to elute earlier than smaller particles.

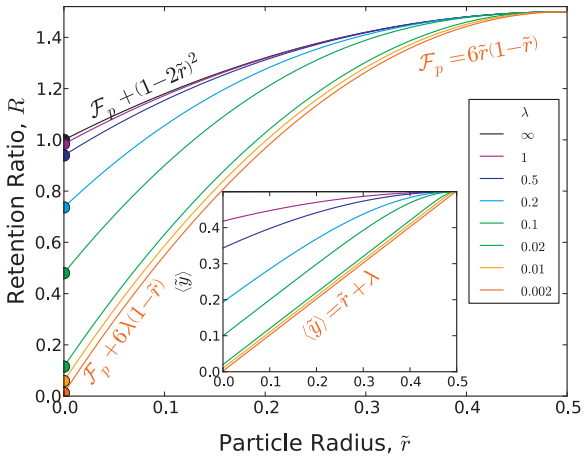

Fig. 4. Retention ratios for a variety of retention parameters varying from small forces of $\lambda = 100$ to large forces of $\lambda = 0.002$. Solid lines denote Eq. (11) and closed circles on the R-axis represent the values predicted by Eq. (7). The inset shows that the mean concentration height $\langle\tilde{y}\rangle$ grows with particle size $\tilde{r}$ when $\lambda \ll 1$.

where $\lambda = \lambda(\tilde{r})$ unless $\alpha = 0$. The concentration distribution controls the mean height

$$\langle\tilde{y}\rangle = \lambda + \frac{1}{1 - e^{(1-2\tilde{r})/\lambda}} + \tilde{r}\coth\left(\frac{1-2\tilde{r}}{2\lambda}\right). \tag{10a}$$

The two limits are now given by

$$\langle\tilde{y}\rangle \simeq \begin{cases} \tilde{r} + \lambda - e^{-(1-2\tilde{r})/\lambda} & \lambda \ll 1 \text{(b)} \\ \dfrac{1}{2}\left[1 - \dfrac{(1-2\tilde{r})^2}{6\lambda} + \dfrac{(1-2\tilde{r})^4}{360\lambda^3} + \cdots\right] \simeq \dfrac{1}{2} & \lambda \gg 1 \text{(c)}. \end{cases} \tag{10}$$

We first note that Eq. (10c) agrees with Eq. (6c) when $\tilde{r} \to 0$, as it should. For strong forces (the small λ case of Eq. (10b)), solute particles are pushed right against the wall and so the mean concentration height is expected to grow linearly with the particle size $\tilde{r}$. This linear relationship is quite evident in mean concentration height for fixed, small values of λ as seen in Eq. (10b) or the inset to Fig. 4. For larger values of λ (weak forces) the solute particles are able to diffuse further from the accumulation wall and the nonlinear terms in Eq. (10a) become apparent in the inset.

As a result of shifting the mean particle height $\langle\tilde{y}\rangle$ towards the centre of the channel by increasing particle size, the mechanism for separation changes to that of *steric-mode* FFF and the retention ratio becomes

$$R(\tilde{r}, \lambda) = 6\lambda\,[1-2\tilde{r}]\,\mathcal{L}\left(\frac{1-2\tilde{r}}{2\lambda}\right) + \mathcal{F}_p, \tag{11}$$

which is strikingly similar to Eq. (7) for normal-mode FFF. The fraction of the channel accessible to the particle, $1-2\tilde{r}$, appears in Eq. (11) while in Eq. (7) it is identically unity. Beyond this effective reduction of channel height, steric effects lead to additional changes to the behaviour of the retention ratio. For convenience of comparison, these effects have been encapsulated into the new term

$$\mathcal{F}_p(\tilde{r}) = 6\tilde{r}(1-\tilde{r}). \tag{12}$$

This result is in agreement with the commonly accepted form [5,34,43]. As seen in Fig. 4, Eq. (7) is the $\tilde{r} \to 0$ limit and so gives the points on the R-intercept of Eq. (11).

Each line in Fig. 4 corresponds to a different λ, held fixed regardless of particle size in spite of the fact that $\lambda = \lambda(\tilde{r})$ (the explicit size dependence of λ will be treated in Section 3.1). Even when λ has no size-dependence, Eq. (11) demonstrates that particles of different sizes can in fact be separated. Historically [34], λ is kept fixed and only the explicit size effects in Eq. (11) are included as is done in

Fig. 4. The present size dependence of Eq. (11) has an interesting consequence for the zero force limit of $\lambda \to \infty$.

2.3. Hydrodynamic chromatography limit

Even in the absence of a field, steric interactions lead to some fractionation as seen by the large λ curves in Fig. 4. The $\lambda \gg 1$ limit represents vanishingly small forces and corresponds to the *hydrodynamic chromatography* [44] limit of FFF [5,20] in which the steric-mode of separation results in retention even when the field is zero.

Since there is no force towards the accumulation wall, the particles have a uniform concentration distribution across the channel with a mean height of $\langle \tilde{y} \rangle = 1/2$. Hydrodynamic chromatography separates particles by excluding them from regions of slow moving solvent near the wall. For a fixed force (fixed λ), this leads to an elution time that decreases with increasing particle size—as opposed to normal-mode FFF as seen in Fig. 2. In Fig. 4, cases of $\lambda \geq 1$ approximate well the hydrodynamic chromatography limit (Eq. (13c)).

The hydrodynamic chromatography limit is only one of four specific limits of Eq. (11):

$$R \simeq \begin{cases} 6\lambda \mathcal{L}\left(\dfrac{1}{2\lambda}\right) & \tilde{r} \to 0 \text{ (a)} \\ \mathcal{F}_p + (1-2\tilde{r})^2 & \tilde{r} \to 1/2 \text{ (b)} \\ \mathcal{F}_p + (1-2\tilde{r})^2 & \lambda \gg 1 \text{ (c)} \\ \mathcal{F}_p + 6\lambda(1-2\tilde{r}) - 12\lambda^2 & \lambda \ll 1 \text{ (d)}. \end{cases} \tag{13}$$

Interestingly, the hydrodynamic chromatography result $\lambda \gg 1$ (Eq. (13c)) also appears when $\tilde{r} \to 1/2$ (Eq. (13b)) reflecting the fact that as the particle size approaches the channel height steric effects will always dominate over the external field (we will return to this limit in Section 3.4). In the limit $\tilde{r} \to 0$, Eq. (11) reduces to Eq. (13a), which is identical to the point-particle prediction of Eq. (7). Each of these limits is marked in Fig. 4. The point-particle limit agrees with the R-intercept and is marked by closed circles while the limits for hydrodynamic chromatography and strong forces are written in.

3. Regimes and transitions

3.1. Transition between normal- and steric-modes

Section 2.2 reviewed the variation of the retention ratio R in a microfluidic channel as a function of particles size $\tilde{r}$ for a fixed retention parameter λ, which is equivalent to a fixed force f regardless of size. This is the manner in which the situation is generally framed in the literature [34]. However, as was broached at the end of Section 2.1, it is generally more reasonable to allow the force to change with particle size. We now incorporate both steric effects and size dependent forces into a unified description by substituting $\lambda = \Lambda \tilde{r}^{-\alpha}$ (Eq. (8)) into the results of Section 2.2. This produces the concentration profile and the retention ratio explicitly in terms of particle size $\tilde{r}$:

$$c(\tilde{y}) = \begin{cases} c_0 e^{-\tilde{r}^\alpha(\tilde{y}-\tilde{r})/\Lambda} & \text{for } \tilde{r} < \tilde{y} < 1-\tilde{r} \\ 0 & \text{otherwise,} \end{cases} \tag{14}$$

$$R(\tilde{r}, \Lambda) = \frac{6\Lambda}{\tilde{r}^\alpha}[1-2\tilde{r}]\,\mathcal{L}\left(\frac{[1-2\tilde{r}]\tilde{r}^\alpha}{2\Lambda}\right) + \mathcal{F}_p(\tilde{r}), \tag{15}$$

while the steric function $\mathcal{F}_p$ remains unchanged from Eq. (12). In these terms, $\alpha = 0$ represents a hypothetical force that is not a function of particle size (as was used in Fig. 4). Fig. 5 shows the retention ratios for a range of Λ when $\alpha = 1$ which is the appropriate scaling for many examples of FFF techniques, as seen in Table 1.

Consider first the extreme particle sizes in Fig. 5. The smallest particle sizes all have a retention ratio approaching $R \to 1$ regardless

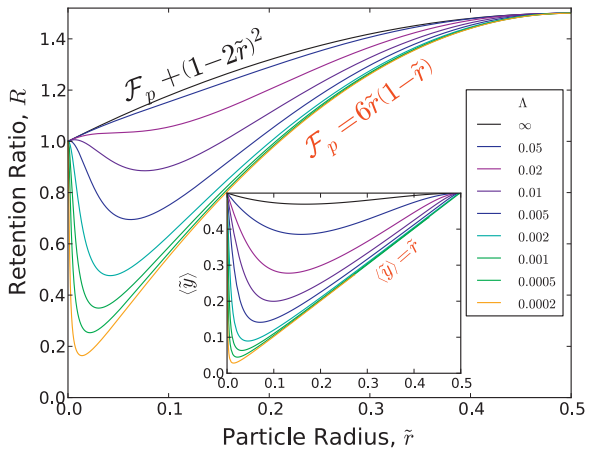

Fig. 5. Retention ratios for $\alpha = 1$. When the force varies as $\tilde{r}^\alpha$, the retention ratio is no longer a simple monotonic rise as it was in Fig. 4 for $\alpha = 0$. Below the critical device retention parameter $\Lambda_c = 1.90 \times 10^{-2}$, the retention ratio becomes nonmonotonic. The insert shows that as Λ decreases, the mean concentration height's minimum occurs at smaller and smaller particle sizes.

of Λ because Brownian motion dominates the applied force. Small $\tilde{r}$ solutes constitute tracer particles which are able to diffuse across the entire channel and sample the entire solvent velocity profile, resulting in $\langle \tilde{y} \rangle = 1/2$ and $R = 1$ for all Λ. Next, consider the largest particle sizes. The inset shows that once again the mean height has become $\langle \tilde{y} \rangle = 1/2$ for all Λ but now the $R \neq 1$. This is because the largest particles fit snugly into the channel causing the concentration distribution to be sharply distributed about $\tilde{y} = 1/2$. The solvent velocity at the centre point is $v\left(1/2\right) = 3\langle v \rangle/2$, which causes the retention ratio to approach $R = 3/2$ as seen in Fig. 5. However, $R \to 3/2$ is physically nonsensical since the speed of such large particles is not well represented by the solvent's velocity in the absence of the particle and so we shall return to this result (see Section 3.4).

Having discussed the extreme points of Fig. 5, we now turn to intermediate values. The most immediately striking property of Fig. 5 is that R is not necessarily a monotonic function of particle size. For large values of Λ, the retention ratio remains monotonic (a perturbation about the hydrodynamic chromatography limit) but when Λ decreases below some critical value Λ_c the retention ratio R becomes nonmonotonic with a minimum at some particle size $\tilde{r}_{NS}(\Lambda)$. Above $\tilde{r}_{NS}$, the retention ratio in Fig. 5 grows in a similar manner as it did in Fig. 4. However, the behaviour of $R(\tilde{r})$ for small particle sizes in the regime $\tilde{r} < \tilde{r}_{NS}$ is much different. At small sizes, as the particle size increases, the retention ratio falls drastically. This is the same behaviour as in Fig. 2 and it is caused by the same mechanisms: As always, the concentration distribution results from the competition between the external field, thermal energy and the hard steric interaction with the wall but at these sizes particles are too small for steric effects to dominate. Instead, in this range the behaviour is the same as that predicted by normal-mode FFF and shown in Fig. 2.

All these properties of R are reflected in the mean concentration height $\langle \tilde{y}(\tilde{r}) \rangle$. The inset of Fig. 5 shows that $\langle \tilde{y}(\tilde{r}) \rangle$ is nonmonotonic with a global minimum for all values of Λ. When Λ is small, the vast majority of particle sizes are above this minimum, and above the minimum the average concentration height increases fairly linearly, $\langle \tilde{y}(\tilde{r}) \rangle \simeq \tilde{r}$. Indeed, in this strong field limit, the external force completely dominates over thermal motion and solute particles are pinned to the accumulation wall. The hard steric repulsion ensures that the mean height of the concentration profile grows linearly with $\tilde{r}$ as it did in Fig. 4. The distribution of particle sizes below

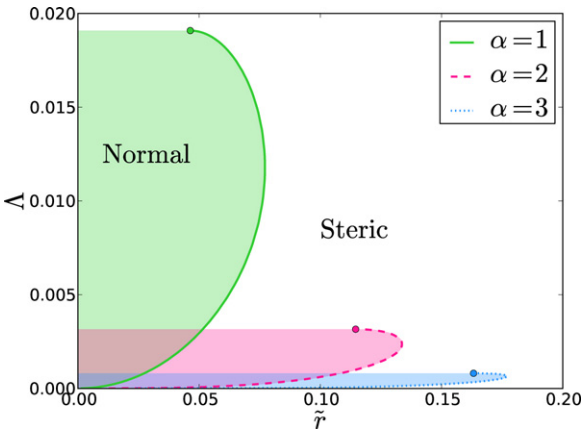

Fig. 6. A tentative operational-mode diagram for FFF (see Figs. 8 and 11). The dividing line between normal-mode FFF and large particle steric-mode FFF is the numerically determined $\tilde{r}_{NS}$. Normal-mode FFF is represented by the shaded regions and does not exist above a critical device retention parameter Λ_c. The critical device retention parameter values ($\Lambda_c = 1.90 \times 10^{-2}$ for $\alpha = 1$; $\Lambda_c = 3.16 \times 10^{-3}$ for $\alpha = 2$; and $\Lambda_c = 8.07 \times 10^{-4}$ for $\alpha = 3$) are marked by a closed circle.

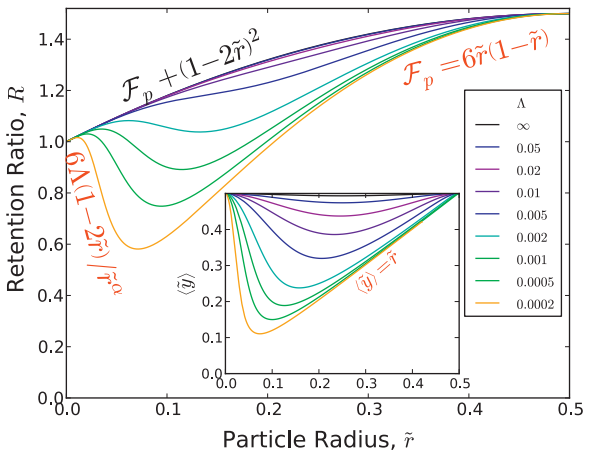

Fig. 7. Retention ratios for $\alpha = 2$. The retention ratio is monotonic above the critical device retention parameter $\Lambda_c = 3.16 \times 10^{-3}$. As discussed in the text, we have three modes of operation when $\Lambda < \Lambda_c$: For the smallest particles the force is negligible, the slope is positive and the mode of operation is hydrodynamic chromatography. For moderately small particles the force dominates, the slope is negative and the mode of operation is normal-mode FFF. For the largest particles the effects of sterically excluded regions are most important, the slope is once again positive and the mode of operation is steric-mode FFF.

the minimum results not from the steric exclusion but from the competition between the force and the thermal noise.

It is this difference in mechanisms that suggests the importance of $\tilde{r}_{NS}$. It is a very generally stated rule in the field of FFF that smaller particles elute before larger particles in normal-mode FFF. On the other hand, in steric-mode FFF larger particles elute before smaller particles [20]. Both modes of operation are considered monotonic and from the definition of $R \propto t_R^{-1}$ in Eq. (2), this rule means that the slope $\partial R/\partial \tilde{r}$ is negative for normal- and positive for steric-mode FFF.

However, it had been intuitively obvious that there must be a transition between the two modes of operation described by Eq. (7) and Eq. (11) (sometimes called the steric-inversion point). Even before we allowed $\lambda \propto \tilde{r}^{-\alpha}$, we saw that Eq. (11) approaches Eq. (7) in the limit $\tilde{r} \to 0$. However, by extracting $\tilde{r}^{-\alpha}$ from λ, we can quantitatively predict $\tilde{r}_{NS}(\Lambda)$, which is in fact the particle size for which this transition occurs as a function of Λ, by numerically finding the minima in Fig. 5 (the roots of $\partial R/\partial \tilde{r}$). The subscript NS was chosen in retrospect to signify that $\tilde{r}_{NS}$ represents the normal-to-steric transition. The transition size is traced in Fig. 6, creating an operational-mode diagram for $\alpha = [1, 2, 3]$.

A transition from normal- to steric-mode FFF exists only below a critical Λ_c. Fig. 6 marks these and the caption lists the numeric values. Above Λ_c there simply is no normal-mode and the retention ratios shown in Fig. 5 monotonically increase with particle size. This will be discussed further in Section 3.2.

3.2. Hydrodynamic chromatography-mode FFF

Section 3.1 used the $\alpha = 1$ case to show that the unified ideal retention theory Eq. (15) can map out the transition between normal- and steric-mode FFF (Fig. 6). However, a careful investigation of Fig. 5 for very small $\tilde{r}$ values when Λ is near Λ_c, (*e.g.* see the $\Lambda = 0.01$ curve) reveals that there is a small region starting at $\tilde{r} = 0$ within which larger particles elute before smaller particles. To investigate this further, consider R for the same set of Λ but with $\alpha = 2$ as shown in Fig. 7.

The transition between normal- and steric-modes (at $\tilde{r} = \tilde{r}_{NS}$) remains; however, a local maximum at $\tilde{r} = \tilde{r}_{HN}$ (with $\tilde{r}_{HN} < \tilde{r}_{NS}$) is clearly evident. Since $\partial R/\partial \tilde{r}$ is positive in the region $\tilde{r} < \tilde{r}_{HN}$, the mode of operation has the same elution order as steric-mode FFF. However, since the thermal forces dominate over the external field in this region, this is actually a small-particle hydrodynamic chromatography regime (hence the subscript HN for the transition between hydrodynamic chromatography and normal-mode FFF).

Normal-mode operation only exists over a range of particle sizes above which steric effects dominate because of the large size of the particle and below which the external force is insignificant due to the particle's small size. This can be seen explicitly in Fig. 8. The normal-mode of operation exists as a lobe when $\Lambda < \Lambda_c$. Above Λ_c, this new small particle hydrodynamic chromatography regime seamlessly transitions directly to steric-mode FFF but below Λ_c, normal-mode FFF exists between the hydrodynamic chromatography- and steric-mode FFF.

A surprising result of Fig. 8 is just how far normal-mode operation can extend along $\tilde{r}$ when the force is a strong function of the particle size. When $\alpha = 3$, normal-mode can be achieved for particle radii as large as 17% the channel height.

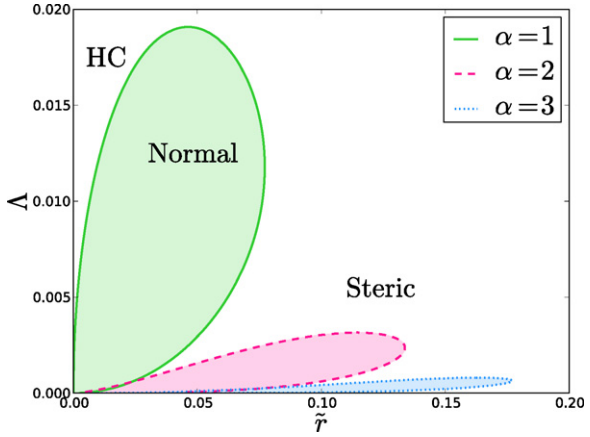

Fig. 8. Enclosed regions are the areas of normal-mode FFF in which smaller particles elute before larger particles. Outer areas are steric-mode and hydrodynamic chromatography limit regions of operation in which larger particles elute before smaller particles. Solid lines are the numerically determined roots of $\partial R/\partial \tilde{r}$ ($\tilde{r}_{HN}$ is a local maximum of R and so forms the left border while $\tilde{r}_{NS}$ is a local minimum and forms the right boarder).

3.3. Limits

Once again it is valuable to consider the limits of the retention ratio. From Eq. (15) we obtain

$$R \simeq \begin{cases} \mathcal{F}_p + (1-2\tilde{r})^2 & \tilde{r} \to 0 \quad \text{(a)} \\ \mathcal{F}_p + (1-2\tilde{r})^2 & \tilde{r} \to 1/2 \quad \text{(b)} \\ \mathcal{F}_p + (1-2\tilde{r})^2 & \Lambda \gg 1 \quad \text{(c)} \\ \mathcal{F}_p + \dfrac{6\Lambda}{\tilde{r}^\alpha}(1-2\tilde{r}) - \dfrac{12\Lambda^2}{\tilde{r}^{2\alpha}} & \Lambda \ll 1. \quad \text{(d)} \end{cases} \tag{16}$$

The hydrodynamic chromatography-mode at the smallest particle sizes that was discussed in Section 3.2 is quadratic in $\tilde{r}$ and is described by Eq. (16a) which is the same limiting behaviour as at large particle sizes (Eq. (16b)) and at large device retention parameters Λ (Eq. (16c)). This is fundamentally different from Eq. (11) in that Eq. (7) can no longer be the point-particle limit since it is impossible to have both extremely small particles and extremely large forces. However, there is no need to assume small particle sizes for the hydrodynamic chromatography. The large $\Lambda \gg 1$ limit of Eq. (16c) is the general hydrodynamic chromatography limit and its form agrees with microfluidic separation studies of hydrodynamic chromatography [45].

The three limits Eqs. (16b)–(16d) are unchanged from the forms in Eq. (13). This has the interesting consequence of making three out of four limits have the form $R \simeq \mathcal{F}_p + (1-2\tilde{r})^2 = 1 + 2\tilde{r} - 2\tilde{r}^2$ which is clear in Fig. 7. The $\tilde{r} \to 0$ and $\tilde{r} \to 1/2$ limits both fall on the hydrodynamic chromatograghy limit of $\Lambda \gg 1$. The anomalous limit is $\Lambda \ll 1$. In fact, inspecting either Fig. 5 or Fig. 7 reveals that this limit itself has two limits.

1 When the particle radius is large, the first term in Eq. (16d) is most important such that $R \approx \mathcal{F}_p = 6\tilde{r}(1-\tilde{r})$. Even at the smallest Λ, as the particle size becomes large all the retention ratios grow in the same manner. The behaviour may seem fairly universal at this point in the discussion but this limit will be improved upon in Section 3.4.
2 When the particle radius is small but the field is extremely strong, (*i.e.* $\Lambda \ll \tilde{r}^\alpha$ or equivalently $\lambda \ll 1$), then the second term in Eq. (16d) dominates meaning that $R \approx 6\Lambda(1-\tilde{r})/\tilde{r}^\alpha \approx 6\lambda$ and the strong force limit from point-particle theory (which is often considered a reasonable approximation [21]) is recovered.

3.4. Faxén-mode FFF

The finite size of the particles has been included as a steric exclusion from the wall but it has a secondary effect as well. Until now, we have considered the velocity of particles whose centres of mass are at some height $\tilde{y}$ to have velocity $\mathcal{V}(\tilde{y}) = v(\tilde{y})$ given by Eq. (3). However, this is not strictly true because the velocity profile is parabolic and so not symmetric about the centre of mass except at $\tilde{y} = 1/2$ [39,46].

The nonphysical consequences are most striking at large particle sizes. As the particle diameter approaches the channel height in Figs. 4, 5 and 7, steric exclusion dominates such that the centre of mass is relegated to the centre of the channel $\tilde{y} = 1/2$ and $c(\tilde{y})$ approaches a Delta-function regardless of the strength of the perpendicular force. The erroneous assumption that even in this limit Eq. (1) does an adequate job approximating particle velocity means that by Eq. (2) the retention ratio becomes

$$R_{1/2} = \lim_{\tilde{r}\to 1/2} R = \frac{\lim_{\tilde{r}\to 1/2}\langle \mathcal{V} \rangle}{\langle v \rangle} = \frac{v\left(\tilde{y} \to 1/2\right)}{\langle v \rangle} = \frac{3}{2}. \tag{17}$$

indicating that the elution time of the largest particles will be significantly shorter than the void time. Intuitively we expect particles that see the entire flow profile to move with the same average velocity as the solvent, *i.e.* $R_{1/2} = 1$. Although it is true that steric effects do dictate the retention ratio regardless of Λ in the large particle limit, continuing to estimate $\lim_{\tilde{r}\to 1/2}\langle \mathcal{V} \rangle$ by it's point-particle value $v\left(\tilde{y} \to 1/2\right)$ becomes increasingly inaccurate. Let us improve upon this assumption.

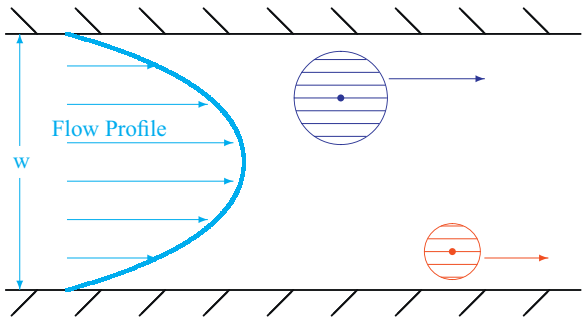

Fig. 9. Schematic of area cross sectional integration of the particle's velocity.

At large sizes a significant portion of the particle's surface sees a much different velocity than $v(\tilde{y})$. Rather than using Eq. (1), a particle's velocity at a position $\tilde{y}$ is better estimated by

$$\langle \mathcal{V} \rangle \cong \frac{\langle \mathcal{V} c \rangle}{\langle c \rangle} \tag{18}$$

where the velocity of the large spherical particles in the presence of the confining walls is no longer estimated by the fluid speed at that point, $\mathcal{V}(\tilde{y}) \neq v(\tilde{y})$. In order to correct for the containing walls, the stress on the sphere must be integrated over it's surface area as schematically shown in Fig. 9. This results in Faxén's Law and gives the velocity of the particle in steady-state to be

$$\mathcal{V}(\tilde{y}) = \left(1 + \frac{\tilde{r}^2}{6}\nabla^2\right) v(\tilde{y}). \tag{19}$$

With this alteration, we can use Eq. (2), Eq. (3), Eq. (9) and Eq. (19) to recalculate the unified ideal retention ratio as

$$\begin{aligned} R(\tilde{r}, \Lambda) &= \frac{1}{\langle v \rangle} \frac{\displaystyle\int_0^w c\mathcal{V} dy}{\displaystyle\int_0^w c dy} \\ &= \frac{6\Lambda}{\tilde{r}^\alpha}[1-2\tilde{r}]\,\mathcal{L}\left(\frac{[1-2\tilde{r}]\,\tilde{r}^\alpha}{2\Lambda}\right) + \mathcal{F}_f(\tilde{r}), \end{aligned} \tag{20}$$

which is identical to Eq. (15) but with a steric function $\mathcal{F}_f$ that is appropriate for finite sized particles. This new steric function $\mathcal{F}_f$ differs trivially from $\mathcal{F}_p$ (given by Eq. (12)) and is

$$\mathcal{F}_f(\tilde{r}) = 6\tilde{r}\left(1 - \frac{4}{3}\tilde{r}\right). \tag{21}$$

Since the form of Eq. (20) is the same as Eq. (15), even the limits on the retention ratio given by Eq. (16) remain robust by simply replacing the steric term $\mathcal{F}_p$ with $\mathcal{F}_f$.

The tiny change from $\mathcal{F}_p$ to $\mathcal{F}_f$ is able to pull the retention ratio for large particles down from $R_{1/2} = 3/2$ to $R_{1/2} = 1$ as seen in Fig. 10 and as is more physically intuitive. Since this region of $\partial R/\partial \tilde{r} < 0$ exists for all Λ and in an ideal theory such as this one the retention ratio must go down to unity, there must always exist a region in the steric-mode regime where $R > 1$.

Fig. 11 traces out the borders between operational-modes. The enclosed, shaded regions represent the normal-mode elution order (smaller particles eluting first) while the unshaded, outer regions operate in the steric-mode elution order (larger particles eluting first). An entirely new region at large $\tilde{r} > \tilde{r}_{SF}$ with normal-mode elution order exists. We call this the *Faxén-mode* FFF regime and so label the transition from steric- to Faxén-mode with the subscript

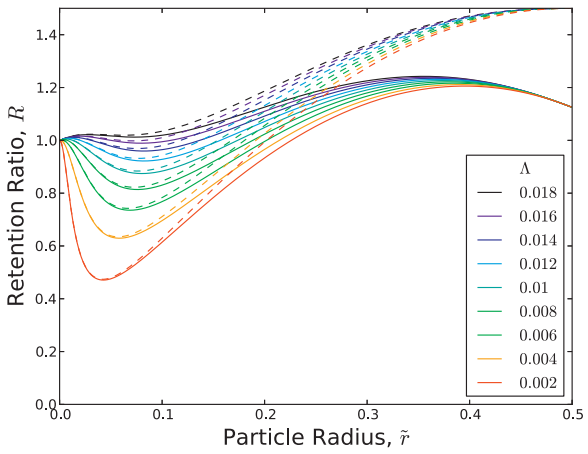

Fig. 10. The retention ratio for $\alpha = 1$ taking into account both steric effects and utilizing Faxén's Law as compared to simply assuming the centre of mass velocity as done previously. Dashed lines correspond to Eq. (15) while solid lines are from Eq. (20) and Eq. (21).

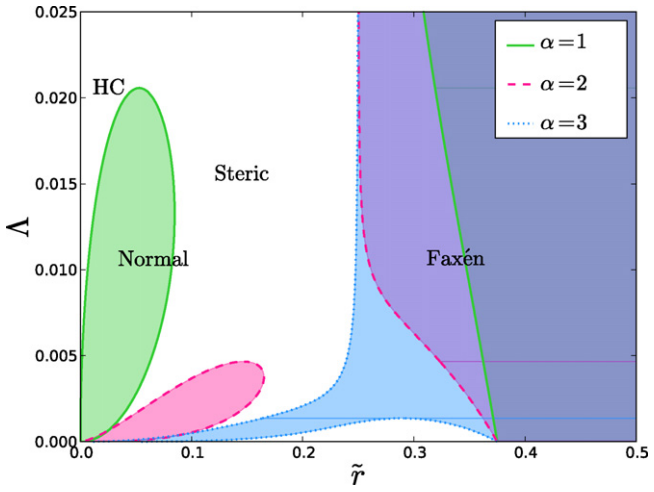

Fig. 11. Ideal FFF-modes map. The numerically determined roots of $\partial R/\partial \tilde{r}$ give the transitions between the four different modes of operation, $\tilde{r}_{HN}$, $\tilde{r}_{NS}$ and $\tilde{r}_{SF}$.

SF. Faxén-mode FFF exists for all Λ. At the largest values of Λ, $\tilde{r}_{SF} \to 0.25$ meaning that the transition occurs when the particle radius is a quarter of the channel height. At smaller Λ, the concentration is biased towards the accumulation wall and the transition doesn't occur until $\tilde{r}_{SF} = 0.375$.

For $\alpha = 1$, 2 the normal-mode and Faxén-mode form disconnected regions while the hydrodynamic chromatography-mode and the steric-mode are a connected space. On the other hand, when $\alpha = 3$ the border between the normal- and steric-modes ($\tilde{r}_{NS}$) extends to such large particle sizes that it passes $\tilde{r}_{SF}$ and so normal-mode interconnects with the Faxén-mode regime. In this case, it is the hydrodynamic chromatography-mode regime of FFF and steric-mode FFF that are disconnected regions.

4. Conclusions

The equations governing the FFF elution time of hard spherical particles in low Reynolds number flow are well known. Eq. (7) is often used for normal-mode FFF while Eq. (11) is used for steric-mode FFF. By explicitly including the external force's dependence on particle size, we are able to quantitatively predict the transition between these two modes of operation. There exists a critical device retention parameter, Λ_c, below which the transition between normal- and steric-mode exists but above which normal-mode operation is not possible.

Furthermore, we find that a mode of operation exists at the smallest particle sizes with the same elution order as steric-mode FFF. The force pushing the particles towards the accumulation wall is size dependent and is insignificant compared to the steric force in this size regime. We quantitatively trace the transition between this small-particle hydrodynamic chromatography-mode FFF and normal-mode FFF. The domain of normal-mode operation only exists as a closed area on the $\Lambda - \tilde{r}$ mode-diagram below Λ_c. Above Λ_c there is no distinction between hydrodynamic chromatography and steric mode-FFF.

By integrating the fluid stress over the surface area of the particles, we further improve the predictions of ideal retention theory for the case of small channel heights (microfluidic devices). The steric function $\mathcal{F}_f$ in the retention ratio is altered but is no more complicated than when this improvement was ignored. The improved expression for the retention ratio predicts a new mode of operation for particles whose diameters approach the channel height. The elution order of this new Faxén-mode FFF is the same as normal-mode FFF and exists for all Λ. When the external force on the particles scales as $\alpha = 3$ (as is true for sedimentation FFF) the normal- and Faxén-mode FFF regimes intersect and form a continuous space.

Accurately predicting the transition points between the four regions can be done through two quadratic equations for the approximate rate of change of the retention ratio with respect to particle size (Eq. (22) and Eq. (24)) in the limiting cases of strong fields or small particle sizes.

FFF can act as a valuable characterization tool in microfluidic devices but the elution time is not necessarily a one-to-one function of particle size. Although this complicates the interpretation of retention profiles, four operational-modes exist, each of which can be utilized to separate samples. By utilizing Fig. 11, one may choose to construct microfluidic channels designed to specifically function in one operational-mode or another for given samples. Doing so would avoid transitions and maintain the retention ratio as a monotonic function of particle size. On the other hand, by using the nonmonotonic form of the retention ratio (Eq. (20)), a microfluidic device need not be limited to a single operational-mode but can be employed to measure all possible particle samples, from relatively tiny tracer particles to particles as large as the microfluidic channel itself.

Nomenclature

c	solute concentration
c_0	solute concentration at the accumulation wall, *i.e.* $c_0 = c(y = r)$
f	external force (perpendicular to flow)
$\mathcal{F}$	steric function in retention ratio
$\mathcal{F}_p$	$\mathcal{F}$ for point-particles
$\mathcal{F}_f$	$\mathcal{F}$ for finite sized particles
$k_B T$	thermal energy
r	particle radius
r_{HN}	transition from hydrodynamic chromatography to normal-mode
r_{NS}	transition from normal- to steric-mode, *i.e.* steric inversion point
r_{SF}	transition from steric- to Faxén-mode
R	retention ratio
$R_{1/2}$	R of largest particle, *i.e.* $R_{1/2} = R\left(r = w/2\right)$
t_0	void time
t_R	retention time
v	solvent velocity

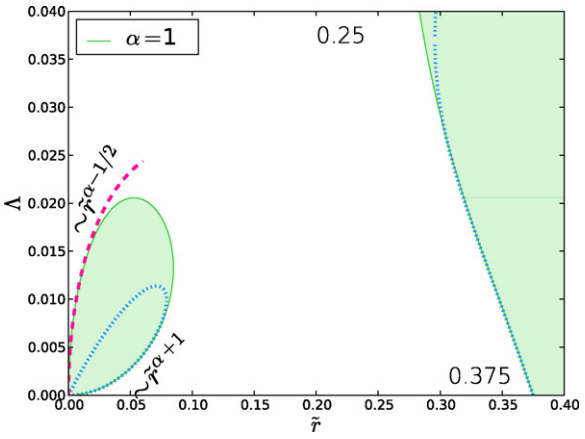

Fig. 12. Approximations to $\tilde{r}_{SF}$ and $\tilde{r}_{NS}$ work well for small device retention parameters Λ as shown by the dotted lines from Eq. (22) for the example of $\alpha = 1$. The dashed line from Eq. (24) shows the small $\tilde{r}$ approximation for the $\tilde{r}_{HN}$ transition.

$\mathcal{V}$	solute velocity
w	channel height
y	distance from the accumulation wall
α	power of force with base r
λ	retention parameter
Λ	device retention parameter, *i.e.* $\Lambda = \lambda\tilde{r}^{\alpha}$
μ	external field
$\tilde{\cdot}$	scaling by channel height
$\langle\cdot\rangle$	cross-sectional average
$\mathcal{L}(\cdot)$	Langevin function

Acknowledgements

We gratefully acknowledge funding by NSERC Discovery Grant to G.W.S. and the NSERC-CGS program to T.N.S. We would also like to thank M.V. Chubynsky and H.W. de Haan for helpful discussions.

Appendix A. Approximations

Although the unified ideal retention ratio is given analytically by Eq. (20), the transitions $\tilde{r}_{HN}$, $\tilde{r}_{NS}$ and $\tilde{r}_{SF}$ must be found numerically from $\partial R/\partial\tilde{r} = 0$. However, in some experimentally relevant limits, the transitions can be well approximated by simple forms.

A.1. Small Λ for $\tilde{r}_{NS}$ and $\tilde{r}_{SF}$

Let us estimate the domain of the normal-mode by taking the small Λ limit of $\partial R/\partial\tilde{r}$ such that the hyperbolic cotangent terms approach unity ($\coth(x) \approx 1$). This results in the approximation

$$\frac{\partial R}{\partial\tilde{r}} \approx 6\left[a + b\Lambda + c\Lambda^2\right] = 0 \tag{22}$$

where

$$a \equiv 1 - \frac{8}{3}\tilde{r}, \qquad b \equiv \frac{2\alpha\tilde{r} - 2\tilde{r} - \alpha}{\tilde{r}^{\alpha+1}}, \qquad c \equiv \frac{4\alpha}{\tilde{r}^{2\alpha+1}}.$$

This has simple, analytic roots. The two roots are plotted in Fig. 12 as dotted lines. Because it is the small Λ limit of $\partial R/\partial\tilde{r}$, Eq. (22) captures the $\tilde{r}_{NS}$ and $\tilde{r}_{SF}$ borders quite well.

To first order, we see from Eq. (22) that the value for which the transition occurs is $\Lambda \approx a/b$ which scales as

$$\Lambda \sim \tilde{r}^{\alpha+1}. \tag{23}$$

It is seen in Fig. 12 that while this small Λ approximation does a poor job estimating the total area of the normal-mode regime, the first root does accurately estimate $\tilde{r}_{NS}$ at small Λ. The second root predicts $\tilde{r}_{SF}$ and agrees exceedingly well in the infinite force limit of $\lim_{\Lambda\to 0}\tilde{r}_{SF} = 3/8 = 0.375$ but cannot approximate the hydrodynamic chromatography limit of $\lim_{\Lambda\to\infty}\tilde{r}_{SF} = 0.25$.

A.2. Small $\tilde{r}$ for $\tilde{r}_{HN}$

The opposite approximation corresponds to the small $\tilde{r}$ values for which the expansion is $\coth(x) \approx x^{-1} + x/3 + x^3/45 + \ldots$. To order $2\alpha + 1$, the rate of change of the retention ratio with particle size is

$$\frac{\partial R}{\partial\tilde{r}} = A + \frac{B}{\Lambda^2} = 0 \tag{24}$$

where

$$A \equiv 2 - 8\tilde{r},$$
$$B \equiv \frac{1}{5}\left[-\frac{\alpha}{6}\tilde{r}^{2\alpha-1} + \frac{2(2\alpha+1)}{3}\tilde{r}^{2\alpha} - 4(\alpha+1)\tilde{r}^{2\alpha+1}\right].$$

Again, the roots to the approximation are simple and have been plotted in Fig. 12 as a dashed line. Despite being a small $\tilde{r}$ approximation, Eq. (24) fails as Λ approaches the critical value Λ_c.

To order $2\alpha + 1$, the value for which the transition occurs is $\Lambda \approx \sqrt{A/B}$ which scales as

$$\Lambda \sim \tilde{r}^{\alpha-1/2}. \tag{25}$$

Interestingly, this scaling means that the concavity of $\tilde{r}_{HN}$ changes with α. When $\alpha = 1$ the normal-mode regime is a "petal" as in Fig. 8 but when $\alpha > 1$ the concavity flips and the normal-mode is more "tear-drop" shaped.

References

[1] T. Rameshwar, S. Samal, S. Lee, S. Kim, J. Cho, I.S. Kim, Determination of the size of water-soluble nanoparticles and quantum dots by field-flow fractionation, J. Nanosci. Nanotechnol. 6 (8) (2006) 2461.
[2] B. Stolpe, M. Hassellöv, Changes in size distribution of fresh water nanoscale colloidal matter and associated elements on mixing with seawater, Geochim. Cosmochim. Acta 71 (13) (2007) 3292.
[3] F. von der Kammer, S. Legros, T. Hofmann, E.H. Larsen, K. Loeschner, Separation and characterization of nanoparticles in complex food and environmental samples by field-flow fractionation, TrAC, Trends Anal. Chem. 30 (3) (2011) 425.
[4] S.K. Ratanathanawongs Williams, J.R. Runyon, A.A. Ashames, Field-flow fractionation: addressing the nano challenge, Anal. Chem. 83 (3) (2011) 634.
[5] J.C. Giddings, M.N. Myers, Steric field-flow fractionation: a new method for separating 1 to 100 μm particles, Sep. Sci. Technol. 13 (8) (1978) 637.
[6] P.S. Williarns, J.C. Giddings, Multifaceted analysis of 0.01 to 100 μm particles by sedimentation field-flow fractionation, Am. Lab. 95 (1993) 88.
[7] C. Claveranne-Lamolère, G. Lespes, S. Dubascoux, J. Aupiais, F. Pointurier, M. Potin-Gautier, Colloidal transport of uranium in soil: size fractionation and characterization by field-flow fractionation-multi-detection, J. Chromatogr., A 1216 (52) (2009) 9113.
[8] M. Lattuada, C. Olivo, C. Gauer, G. Storti, M. Morbidelli, Application of asymmetric flow-field flow fractionation to the characterization of colloidal dispersions undergoing aggregation, Langmuir 26 (10) (2010) 7062.
[9] M. Baalousha, B. Stolpe, J.R. Lead, Flow field-flow fractionation for the analysis and characterization of natural colloids and manufactured nanoparticles in environmental systems: a critical review, J. Chromatogr., A 1218 (27) (2011) 4078.
[10] A.R. Poda, A.J. Bednar, A.J. Kennedy, A. Harmon, M. Hull, D.M. Mitrano, J.F. Ranville, J. Steevens, Characterization of silver nanoparticles using flow-field flow fractionation interfaced to inductively coupled plasma mass spectrometry, J. Chromatogr., A 1218 (27) (2011) 4219.
[11] S.K. Ratanathanawongs Williams, D. Lee, Field-flow fractionation of proteins, polysaccharides, synthetic polymers, and supramolecular assemblies, J. Sep. Sci. 29 (12) (2006) 1720.
[12] C. Scherer, S. Noskov, S. Utech, C. Bantz, W. Mueller, K. Krohne, M. Maskos, Characterization of polymer nanoparticles by asymmetrical flow field flow fractionation (af-fff), J. Nanosci. Nanotechnol. 10 (10) (2010) 6834.
[13] J.R. Runyon, S.K. Ratanathanawongs Williams, Composition and molecular weight analysis of styrene-acrylic copolymers using thermal field-flow fractionation, J. Chromatogr., A 1218 (38) (2011) 6774.
[14] J.R. Runyon, S.K. Ratanathanawongs Williams, A theory-based approach to thermal field-flow fractionation of polyacrylates, J. Chromatogr., A 1218 (39) (2011) 7016.

[15] R. Qureshi, W. Kok, Application of flow field-flow fractionation for the characterization of macromolecules of biological interest: a review, Anal. Bioanal. Chem. 399 (2011) 1401, doi:10.1007/s00216-010-4278-3.
[16] H. Lee, S.K. Ratanathanawongs Williams, K.L. Wahl, N.B. Valentine, Analysis of whole bacterial cells by flow field-flow fractionation and matrix-assisted laser desorption/ionization time-of-flight mass spectrometry, Anal. Chem. 75 (11) (2003) 2746.
[17] J. Vykoukal, D.M. Vykoukal, S. Freyberg, E.U. Alt, P.R.C. Gascoyne, Enrichment of putative stem cells from adipose tissue using dielectrophoretic field-flow fractionation, Lab Chip 8 (2008) 1386.
[18] P.R.C. Gascoyne, J. Noshari, T.J. Anderson, F.F. Becker, Isolation of rare cells from cell mixtures by dielectrophoresis, Electrophoresis 30 (8) (2009) 1388.
[19] L.F. Pease, D.I. Lipin, D.-H. Tsai, M.R. Zachariah, L.H.L. Lua, M.J. Tarlov, A.P.J. Middelberg, Quantitative characterization of virus-like particles by asymmetrical flow field flow fractionation, electrospray differential mobility analysis, and transmission electron microscopy, Biotechnol. Bioeng. 102 (3) (2009) 845.
[20] H. Cölfen, M. Antonietti, New Developments in Polymer Analytics I, volume 150 of Advances in Polymer Science, chapter Field-Flow Fractionation Techniques for Polymer and Colloid Analysis, Springer, Berlin/Heidelberg, 2000, p. 67.
[21] F.A. Messaud, R.D. Sanderson, J.R. Runyon, T. Otte, H. Pasch, S.K. Ratanathanawongs Williams, An overview on field-flow fractionation techniques and their applications in the separation and characterization of polymers, Prog. Polym. Sci. 34 (4) (2009) 351.
[22] B.K. Gale, K.D. Caldwell, A.B. Frazier, A micromachined electrical field-flow fractionation (μ-EFFF) system, IEEE Trans. Biomed. Eng. 45 (12) (1998) 1459.
[23] A. Kantak, M. Srinivas, B. Gale, Characterization of a microscale cyclical electrical field flow fractionation system, Lab Chip 6 (5) (2006) 645.
[24] Y. Huang, X.B. Wang, F.F. Becker, P.R. Gascoyne, Introducing dielectrophoresis as a new force field for field-flow fractionation, Biophys. J. 73 (2) (1997) 1118.
[25] X.B. Wang, J. Yang, Y. Huang, J. Vykoukal, F.F. Becker, P.R.C. Gascoyne, Cell separation by dielectrophoretic field-flow-fractionation, Anal. Chem. 72 (4) (2000) 832.
[26] T.L. Edwards, B.K. Gale, A.B. Frazier, A microfabricated thermal field-flow fractionation system, Anal. Chem. 74 (6) (2002) 1211.
[27] S. Bargiel, A. Górecka-Drzazga, J.A. Dziuban, A micromachined system for the separation of molecules using thermal field-flow fractionation method, Sens. Actuators, A 110 (1–3) (2004) 328.
[28] H. Sant, B. Gale, Microscale field-flow fractionation: theory and practice, in: Steffen Hardt, Friedhelm Schönfeld (Eds.), Microfluidic Technologies for Miniaturized Analysis Systems, Springer, USA, 2007, p. 471.
[29] B.K. Gale, H.J. Sant, Nanoparticle analysis using microscale field flow fractionation, in: SPIE Conference Series, vol. 6465, 2007, p. 18.
[30] J.C. Giddings, Micro-FFF: theoretical and practical aspects of reducing the dimensions of field-flow fractionation channels, J. Microcolumn Sep. 5 (6) (1993) 497.
[31] B.K. Gale, K.D. Caldwell, A.B. Frazier, Geometric scaling effects in electrical field flow fractionation. 1. Theoretical analysis, Anal. Chem. 73 (10) (2001) 2345.
[32] H.J. Sant, B.K. Gale, Geometric scaling effects on instrumental plate height in field flow fractionation, J. Chromatogr., A 1104 (1–2) (2006) 282.
[33] J.C. Giddings, Nonequilibrium theory of field-flow fractionation, J. Chem. Phys. 49 (1) (1968) 81.
[34] J.C. Giddings, Displacement and dispersion of particles of finite size in flow channels with lateral forces. Field-flow fractionation and hydrodynamic chromatography, Sep. Sci. Technol. 13 (3) (1978) 241.
[35] M. Martin, Deviations to classical retention theory of field-flow fractionation, J. Chromatogr., A 831 (1) (1999) 73.
[36] G. Westermann-Clark, Note on nonisothermal flow in field-flow fractionation, Sep. Sci. Technol. 13 (9) (1978) 819.
[37] J.E. Belgaied, M. Hoyos, M. Martin, Velocity profiles in thermal field-flow fractionation, J. Chromatogr., A 678 (1) (1994) 85.
[38] P.S. Williams, S. Lee, J.C. Giddings, Characterization of hydrodynamic lift forces by field-flow fractionation. Inertial and near-wall lift forces, Chem. Eng. Commun. (1994).
[39] P.S. Williams, M.H. Moon, J.C. Giddings, Influence of accumulation wall and carrier solution composition on lift force in sedimentation/steric field-flow fractionation, Colloids Surf., A 113 (3) (1996) 215.
[40] D. Di Carlo, D. Irimia, R.G. Tompkins, M. Toner, Continuous inertial focusing, ordering, and separation of particles in microchannels, Proc. Natl. Acad. Sci. U.S.A. 104 (48) (2007) 18892.
[41] M. Martin, F. Feuillebois, Onset of sample concentration effects on retention in field-flow fractionation, J. Sep. Sci. 26 (6–7) (2003) 471.
[42] D. Di Carlo, J.F. Edd, D. Irimia, R.G. Tompkins, M. Toner, Equilibrium separation and filtration of particles using differential inertial focusing, Anal. Chem. 80 (6) (2008) 2204, PMID: 18275222.
[43] F.R. Phelan Jr., B.J. Bauer, Comparison of steric effects in the modeling of spheres and rodlike particles in field-flow fractionation, Chem. Eng. Sci. 64 (8) (2009) 1747.
[44] H. Small, Hydrodynamic chromatography a technique for size analysis of colloidal particles, J. Colloid Interface Sci. 48 (1) (1974) 147.
[45] Y. Wang, W. Jiang, S. Miller, E. Eckstein, Dissipative particle dynamics simulation of on-chip hydrodynamic chromatography, J. Chromatogr., A 1198–1199 (0) (2008) 140.
[46] D. Di Carlo, J.F. Edd, K.J. Humphry, H.A. Stone, M. Toner, Particle segregation and dynamics in confined flows, Phys. Rev. Lett. 102 (March (9)) (2009) 094503.